Electronic Supplementary Information for

Pushing slope- to plateau-type behavior in hard carbon for sodium-ion batteries *via* local structure rearrangement

Feng Wang,[a,b]# Lian Chen,[a] # Jiaqi Wei,[c] Caozheng Diao,[d] Fan Li,[b] Congcong Du,[a] Zhengshuai Bai,[b] Yanyan Zhang,[b] Oleksandr I. Malyi,*[a,e] Xiaodong Chen,[c] Yuxin Tang,*[a,b] Xiaojun Bao*[a,b]

[a] Dr. F. Wang, Dr. L. Chen, Dr. C. Du, Dr. O. I. Malyi, Prof. Y. Tang, Prof. X. Bao
Qingyuan Innovation Laboratory, 1 Xueyuan Road, Quanzhou 362801, P. R. China
E-mail: oleksandrmalyi@gmail.com

[b] Dr. F. Wang, F. Li, Prof. Z. Bai, Prof. Y. Zhang, Prof. Y. Tang, Prof. X. Bao
College of Chemical Engineering, Fuzhou University, Fuzhou 350116, P. R. China
E-mail: yxtang@fzu.edu.cn; baoxj@fzu.edu.cn

[c] Dr. J. Wei, Prof. X. Chen
Innovative Centre for Flexible Devices (iFLEX), School of Materials Science and Engineering, Nanyang Technological University, 50 Nanyang Avenue, Singapore, 639798 Singapore

[d] Dr. C. Diao
Singapore Synchrotron Light Source, National University of Singapore, 5 Research Link, Singapore, 117603 Singapore

[e] Dr. O. I. Malyi
Centre of Excellence ENSEMBLE3 Sp. z o. o., Wolczynska Str. 133, 01-919, Warsaw, Poland

#These two authors contribute equally to this work.

Experimental Section

Methods

Preparation of the hard carbon anode

The hard carbon was synthesized by different temperature gradient protocols. In detail, the wood precursor from the poplar (bought from www.taoobao.com) stabilized the temperature gradient at 800, 1300, 1500, and 1900°C (5 °C/min) for 3 hours under an argon environment, respectively, which makes it possible to determine the structural information and track the formation mechanism. Inspired by the clothing size, we named the microstructure parameter in order, including (i): the large d_{002} (d_{xl}), large defect density (D_l) and small layer of L_a (L_s), (ii): the medium d_{002} (d_m), medium defect density (D_m), and medium layer of L_a (L_m), (iii): the small d_{002} (d_s), small defect density (D_s), and large layer of L_a (L_l), (iv): the extra-small d_{002} (d_{xs}), extra-small defect density (D_{xs}), and extra-large layer of L_a (L_{xl}), and corresponding to the as-prepared hard carbon samples of $d_lD_lL_s$, $d_mD_mL_m$, $d_sD_sL_l$, and $d_{xs}D_{xs}L_{xl}$, respectively. To obtain a control sample, the wood precursor is stabilized at 500 °C (5 °C/min) for 3 hours under an argon environment with the extra-large d_{002} (d_{xl}), extra-large defect density (D_{xl}) and small layer of L_a (L_{xs}), denoted as $d_{xl}D_{xl}L_{xs}$.

Electrochemical measurements

The electrochemical performance of all electrodes was examined using coin-type (type CR20232) cells with sodium foil as a counter. All hard carbon electrode materials were prepared by mixing active material, sodium carboxymethyl cellulose, and Super P, and (90:5:5) onto a copper foil current collector, which has an average mass loading of approximately 2-3 mg cm^{-2} without gas protection; 1 M $NaPF_6$ in glyme (DME) was used as the electrolyte and a glass fiber film (Whatman GF/A) was used as the separator. Galvanostatic charge and discharge measurements at different current densities and galvanostatic intermittent titration technique (GITT) were carried out on a battery controlling system (Newaretester BTS-610) in a voltage range from 2.0 to 0.005 V (versus Na/Na$^+$). Cyclic voltammetry (CV) and Electrochemical impedance spectroscopy (EIS) measurements were carried out by a cell test system (Par-solartron 1400). All the electrochemical measurements above were conducted at 25 °C. The overall GITT profile of hard carbon electrodes during charge and discharge with a pulse current at 50 mA g^{-1} for

10 min between rest intervals for 120 min. Use the following equation to calculate D_{Na^+}:

$$D_{Na} = \frac{4}{\pi t}\left(\frac{mV}{MS}\right)^2\left(\frac{\Delta E_s}{\Delta E_t}\right)^2 \quad (t << \frac{l^2}{D_{Na}}) \qquad \text{S1}$$

where τ stands for the period of the current pulse at a specific current density; m, M, V, S, and l represent the mass loading, the molecular weight, the molar volume, the electrode contact area, and the thickness, respectively.

Materials characterization

X-ray diffraction (XRD, Rigaku D/Max 2500, Japan) was conducted to study the crystal structure and phase composition. Raman spectra were collected from a Raman spectrometer (Jobin Yvon, HR800) with a 532 nm laser beam. X-ray photoelectron spectra (XPS) were performed on a KRATOS Axis Ultra-X-ray photoelectron spectrometer with a mono-chromicized Al Kα radiation at 225 W. N_2 adsorption-desorption was performed using the BELSORP MAX analyzer. The pycnometry experiments of the prepared hard carbons were conducted on BELPycno (MicrotracBEL Japan, Inc.) to detect the skeletal density. True density analysis and the small angle X-ray scattering (SAXS) technique were elevated for the closed pore structure by a Rigaku 3.5 m NANOPIX system equipped with a Cu kα radiation source. The TOF-SIMS measurements were conducted using a TOF-SIMS IV (ION-TOF GmbH, Germany) with a bismuth liquid metal ion source (25 keV). The analysis area was 200×200 μm^2. Depth profiles were obtained by sputtering with a Cs^+ ion beam (1 keV). The composition of the SEI was investigated by XPS, Thermo Scientific K-Alpha, with depth profiling on HC electrodes after 50 cycles at 50 mA g^{-1}. Note that the denoted etching depth was roughly calculated based on the Ar^+ etching time. In-situ EIS for three electrode HC cells was performed using solartron metrology in a frequency range of 10^2-10^6 Hz at 25 °C.

DRT and DCT analysis: The distribution of relaxation times (DRT) and the distribution of capacitive times (DCT) were used to unravel various processes in the hard carbon cells.

DRT and DCT deconvolution used the impedance and admittance data, respectively. DRT impedance, Z_{DRT} (f), at a frequency f, can be expressed as[1]

$$Z_{DRT}\ (f) = i2\pi f\,L_0 + R\infty + \int_{-\infty}^{+\infty} \frac{\gamma(log\tau)}{1 + i2\pi f\,\tau}dlog\,\tau \qquad \text{S2}$$

where L_0, $R\infty$, τ, and $\gamma(log\tau)$ are an inductance, an ohmic resistance, a timescale, and the DRT, respectively. In turn, the total polarization resistance, R_{pol}, was computed using the following integral:

$$Rpol = \int_{-\infty}^{+\infty} \gamma(log\tau)dlog\,\tau \qquad \text{S3}$$

The DRT analysis was conducted as reported previously[2] with a regularization parameter of 0.001. The DCT admittance, $Y_{DCT}\ (f)$, at a frequency f, is given by[3]

$$Y_{DCT}\ (f) = i2\pi f\,C_0 + G\infty + i2\pi f \int_{-\infty}^{+\infty} \frac{\gamma_{DCT}(log\tau)}{1 + i2\pi f\,\tau}dlog\,\tau \qquad \text{S4}$$

where C_0, $G\infty$, and $\gamma_{DCT}(log\,\tau)$ are capacitance, ohmic conductance, and DCT, respectively. The total conductance, $G_{S,tot}$, is given by:

$$G_{S,tot} = f \int_{-\infty}^{+\infty} \gamma_{DCT}\ (log\,\tau)\ dlog\,\tau \qquad \text{S5}$$

In-situ Raman and in-situ XRD for hard carbon

The hard carbon electrodes were prepared using 90 wt.% active materials and 10 wt.% polytetrafluoroethylene (PTFE) with a mass loading of 10 mg cm-2. A thin quartz window with a thickness of 0.5 mm was fixed on the top of the in-situ Raman cells, and signals were collected through the quartz window. The in-situ cell was tested using a beryllium window for XRD. The in-situ cells were tested in the potential range of 0.005-2.0 V at a constant current density of 50 mA g^{-1}.

**Ex-situ synchrotron X-ray absorption spectroscopy for hard carbon**

The *ex-situ XAS measurements were performed by carefully disassembling the* hard carbon of $d_sD_sL_l$ cells with different states of charge/discharge in an argon-filled glovebox (H_2O < 1 ppm, O_2 < 1 ppm). The electrodes were soaked in anhydrous glyme for 2 h to remove Na salts and/or a thick SEI layer that prohibits the detailed analysis of XAS. The samples were transferred to the Soft X-ray-Ultraviolet (SUV) beamline of the Singapore Synchrotron Light Source for the synchrotron X-ray measurements. The Na and O K-edge XAS spectroscopy were performed at

room temperature and after overnight ultrahigh vacuum (10^{-8} Pa) stabilization. Total electron yield mode XAS was conducted in 520-560 eV with 0.1 eV energy step for O K edge measurement, 1060-1140 eV with 0.1 eV energy step for Na K edge XANES, and 1060-1500 eV with 1 eV energy step for Na K edge EXAFS.

First-principles calculations: To understand the role of local structure on Na storage properties, density functional theory (DFT) calculations were performed using the Vienna Ab initio Simulation Package (VASP)[4-7] with optB86b-vdW functional[8]. For plane wave basis, the cutoff energy levels were set to 400 and 520 eV for main calculations and volume relaxation, respectively. To demonstrate the role of different local structures on Na storage, Na interaction with bilayer graphene was described for different interlayer separations. Here, to maintain interlayer separation, distance no C atom relaxation in the vertical direction was allowed. The relaxation for all other atoms was fully allowed until the intrinsic forces were below 0.01 eV/Å. The bilayer graphene calculations were performed for the 144-atom supercell. To understand the role of point defect on the Na storage, Na interaction with C vacancy of graphene was calculated in 72-atom C supercells. For these defect structures, all atoms were fully relaxed with the same force convergence criterion as in the bilayer graphene system. The Γ-centered Monkhorst−Pack k-grid of 4×4×1 was used for all the calculations. To understand under which a specific local structure contributes to voltage, the voltage was calculated as

$$V_s = -\,(E_{Na+C} - E_C - E_{Na})/e$$

where e, E_{Na+C}, E_C, and E_{Na} are electron charge, total energies of single Na in a given local structure, given local structure, and metallic Na, respectively. The results were analyzed using pymatgen[9] and Vesta[10].
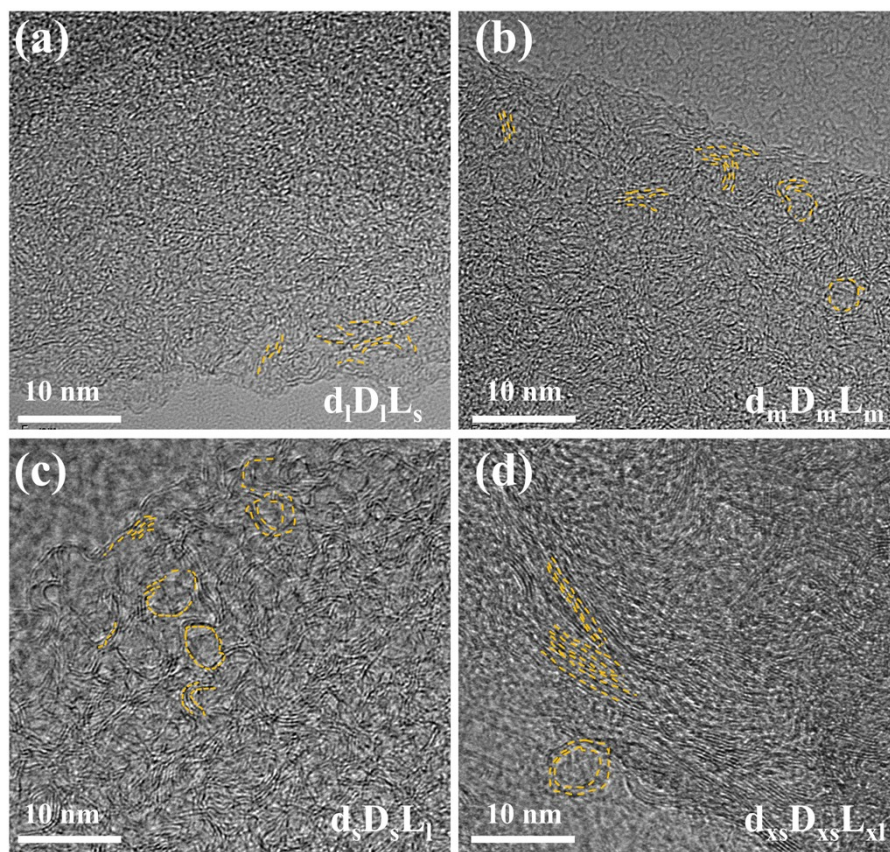
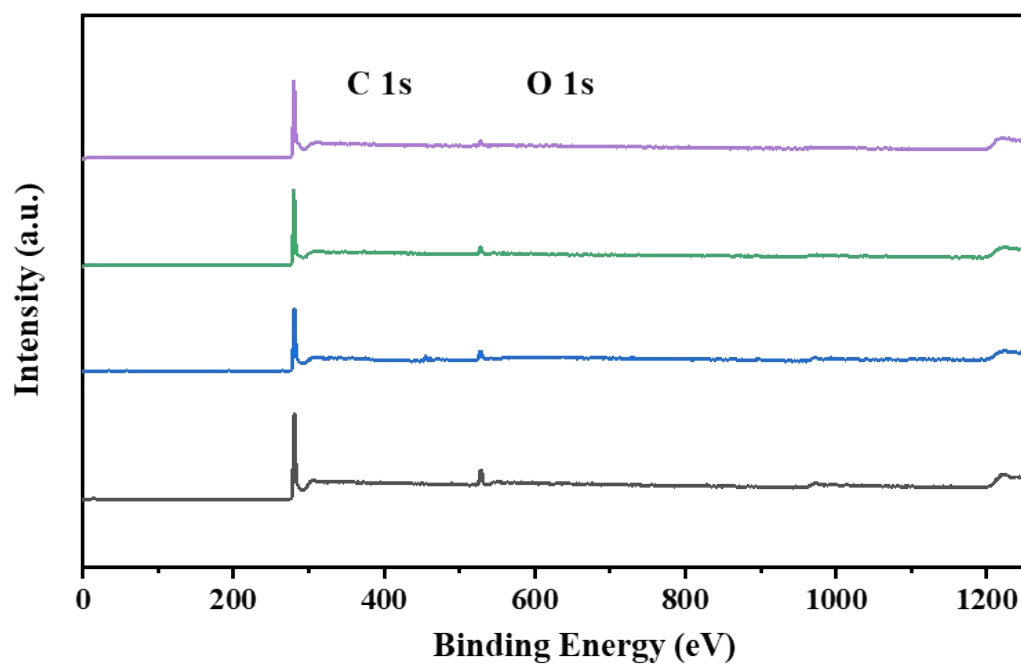**Figure S1.** TEM images of the $d_lD_lL_s$, $d_mD_mL_m$, $d_sD_sL_l$, and $d_{xs}D_{xs}L_{xl}$ samples.
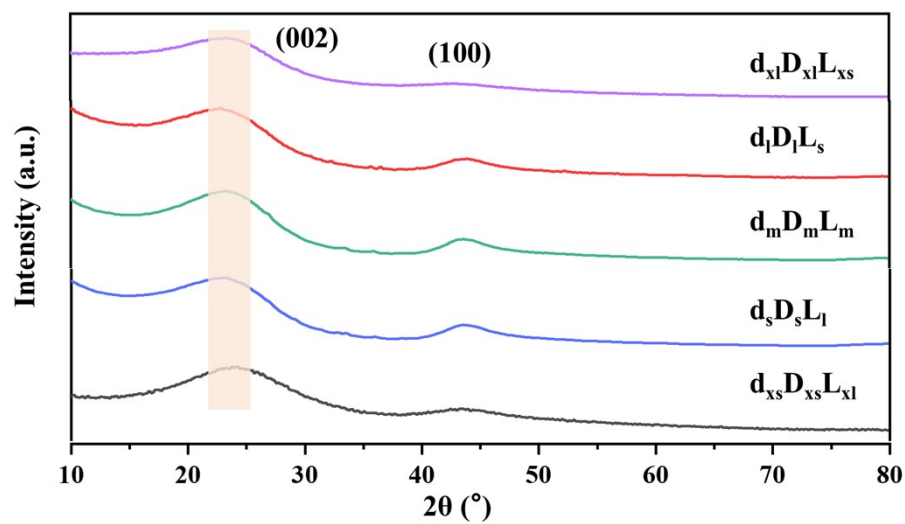
Figure S2. X-ray diffraction (XRD) patterns of the $d_{xl}D_{xl}L_{xs}$, $d_lD_lL_s$, $d_mD_mL_m$, $d_sD_sL_l$, and $d_{xs}D_{xs}L_{xl}$ samples.
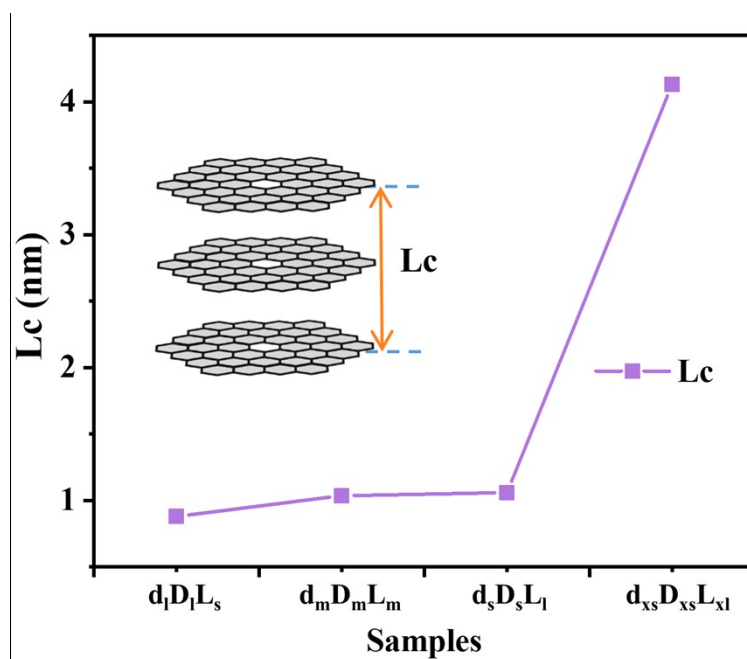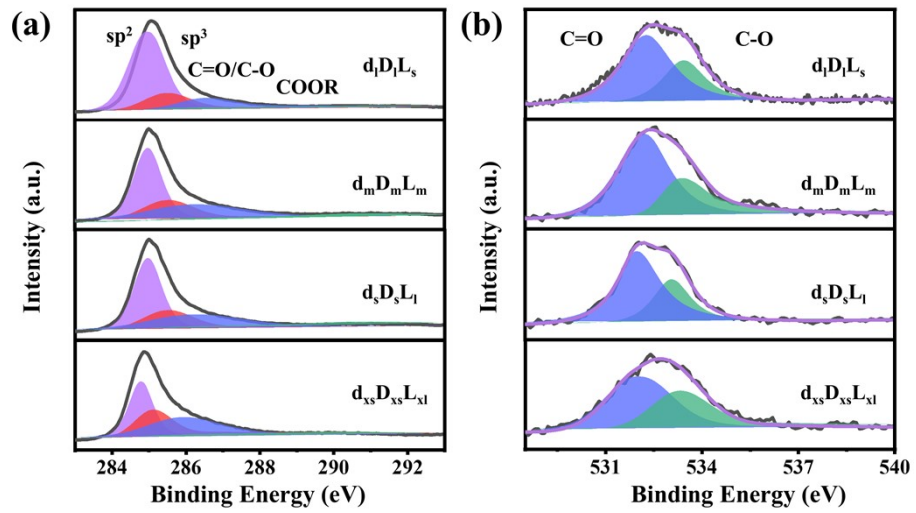
Figure S3. The average crystallite thickness (L_c) graphitic domains of X-ray diffraction (XRD) patterns for the $d_lD_lL_s$, $d_mD_mL_m$, $d_sD_sL_l$, and $d_{xs}D_{xs}L_{xl}$ samples.
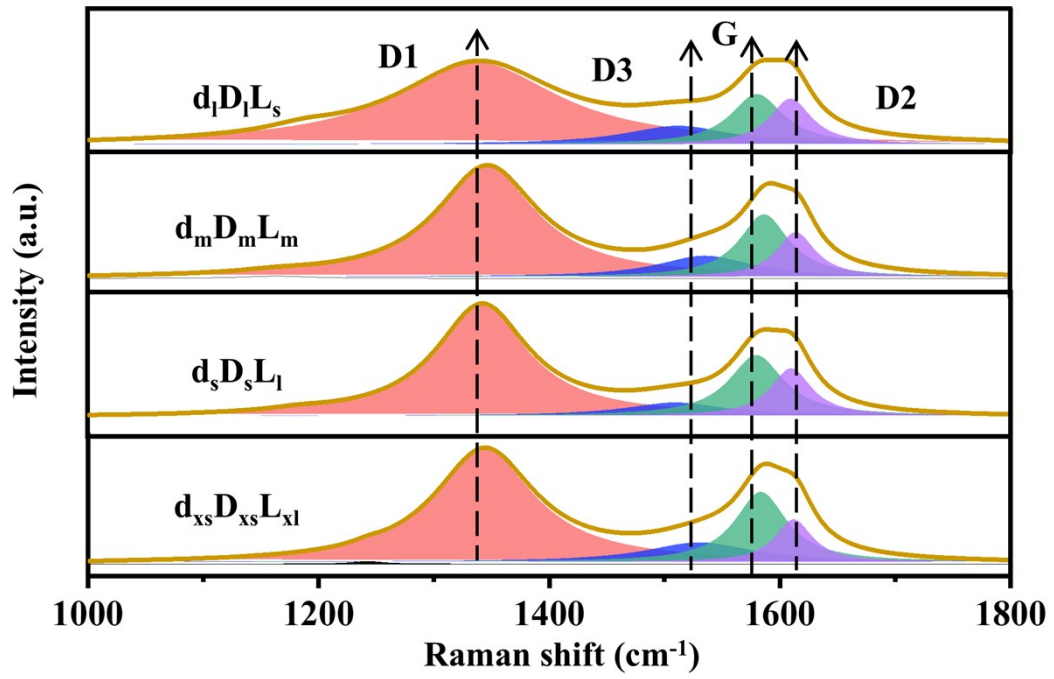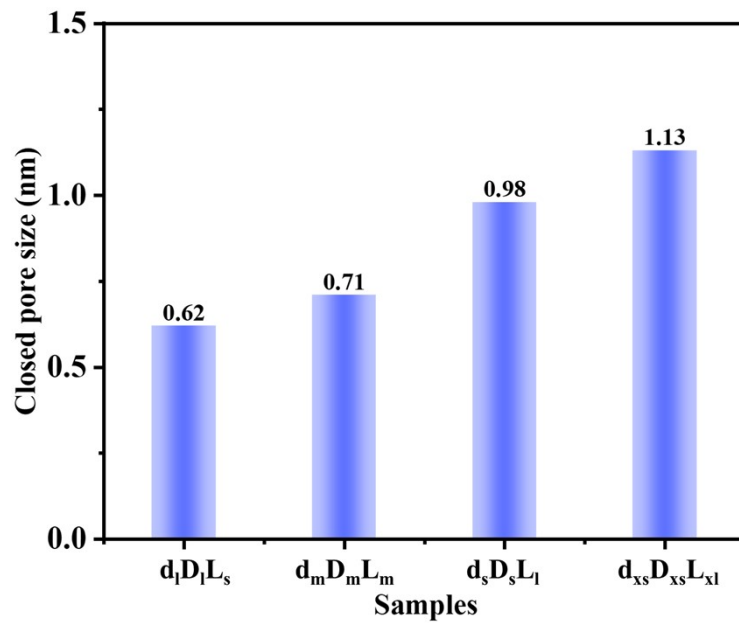
**Figure S4.** Wide-range X-ray photoelectron spectroscopy (XPS) spectra comparison of the $d_lD_lL_s$, $d_mD_mL_m$, $d_sD_sL_l$, and $d_{xs}D_{xs}L_{xl}$ samples.

Figure S5. X-ray photoelectron spectroscopy (XPS) of (a) C1s and (b) O1s spectra comparison of the $d_lD_lL_s$, $d_mD_mL_m$, $d_sD_sL_l$, and $d_{xs}D_{xs}L_{xl}$ samples.
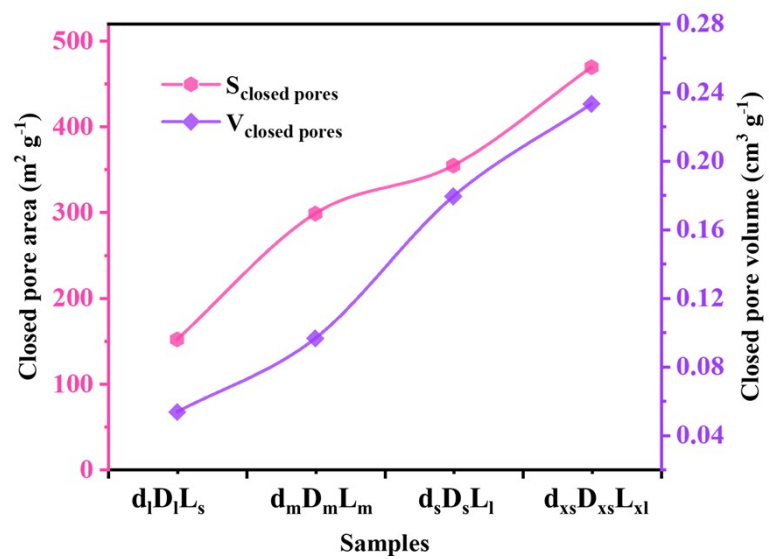
Figure S6. Raman spectra of the $d_lD_lL_s$, $d_mD_mL_m$, $d_sD_sL_l$, and $d_{xs}D_{xs}L_{xl}$ samples.

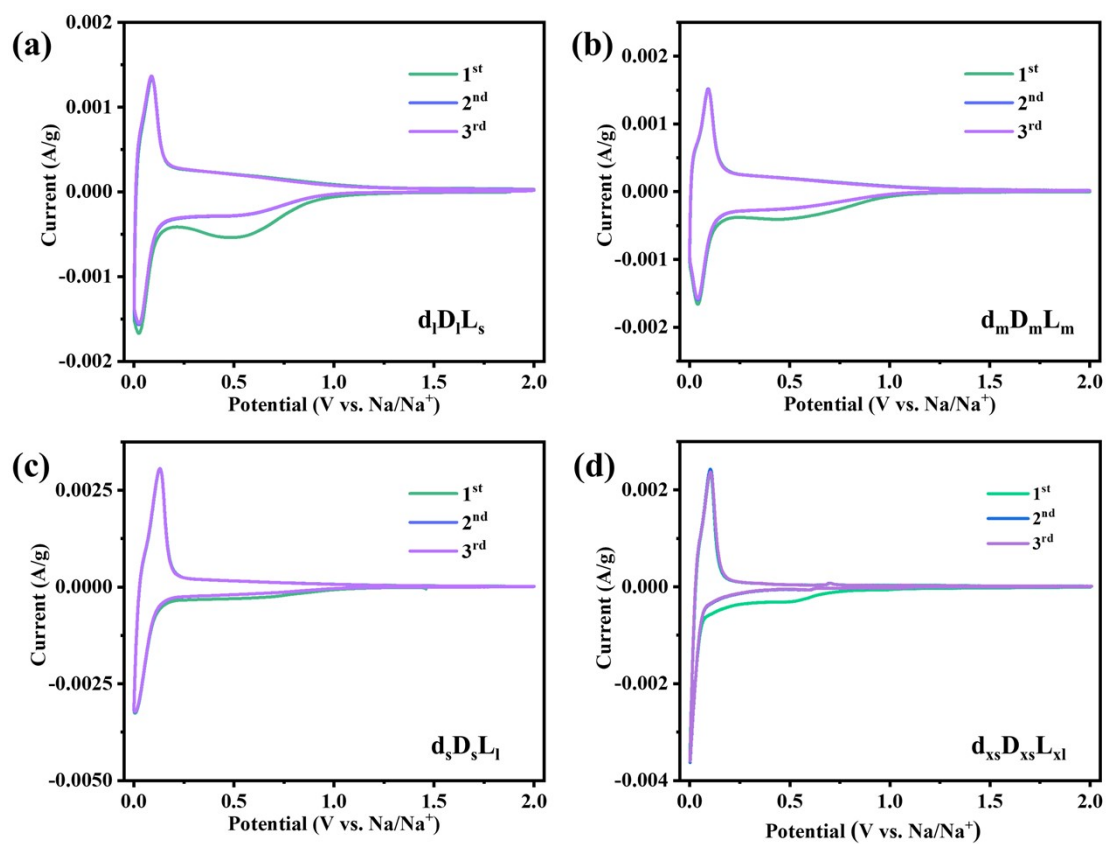**Figure S7.** The closed pore size of the $d_lD_lL_s$, $d_mD_mL_m$, $d_sD_sL_l$, and $d_{xs}D_{xs}L_{xl}$ samples by the SAXS View.
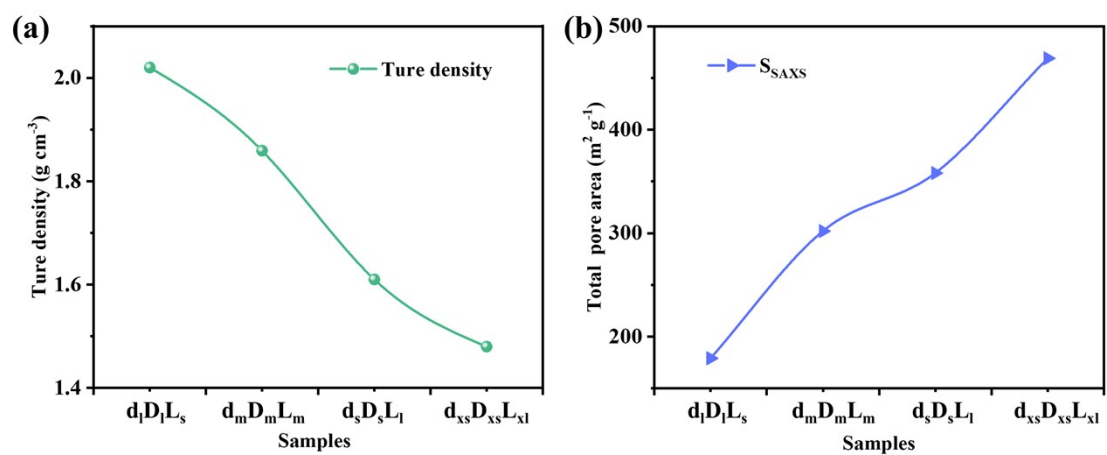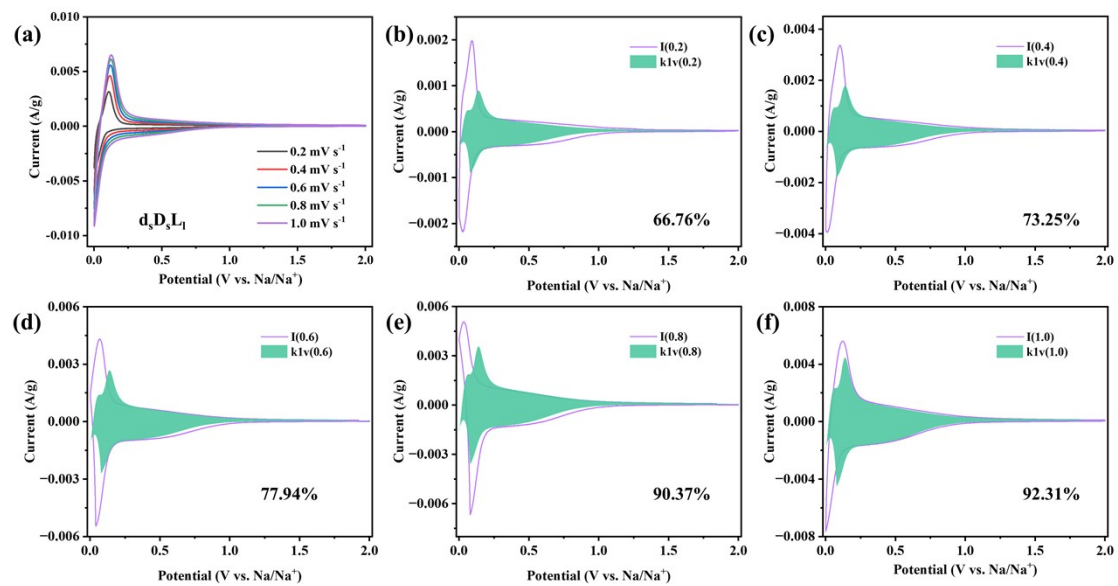
Figure S8. (a) True density and (b) total pore area of the $d_lD_lL_s$, $d_mD_mL_m$, $d_sD_sL_l$, and $d_{xs}D_{xs}L_{xl}$ samples.

Figure S9. The closed pore area and closed pore volume of the $d_lD_lL_s$, $d_mD_mL_m$, $d_sD_sL_l$, and $d_{xs}D_{xs}L_{xl}$ samples.
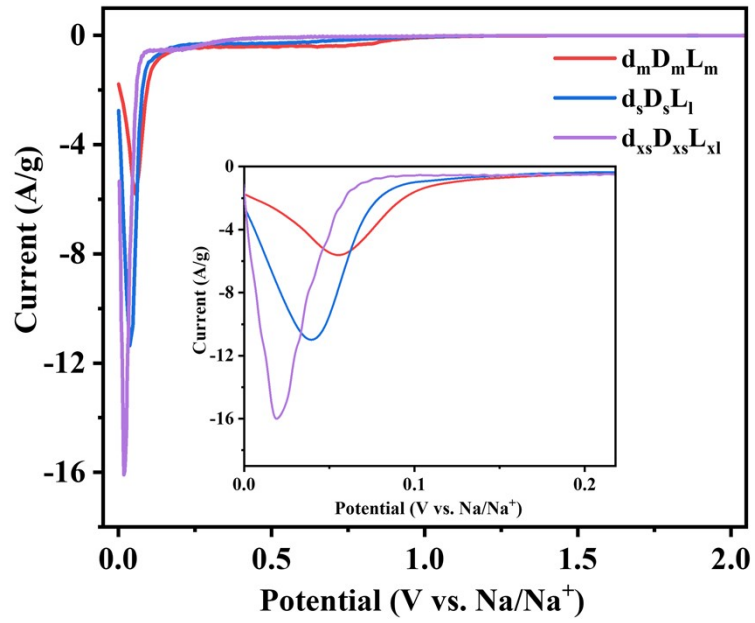
Figure S10. (a-d) CV curves at a scan rate of 0.02 mV s^{-1} of the $d_lD_lL_s$, $d_mD_mL_m$, $d_sD_sL_l$, and $d_{xs}D_{xs}L_{xl}$ samples in the 3rd cycles.
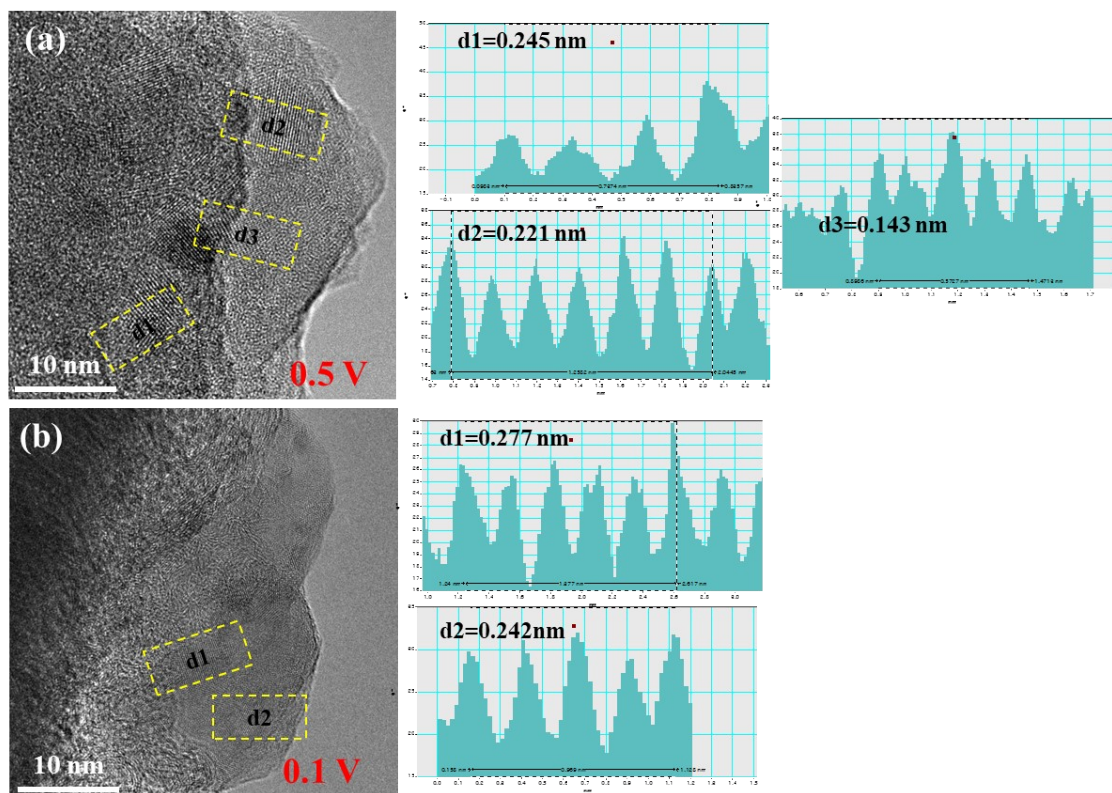
Figure S11. CV curves at different scan rates of the $d_sD_sL_l$ electrode, and corresponding to the normalized contribution ratio of the capacitive-controlled process at various scan rates.
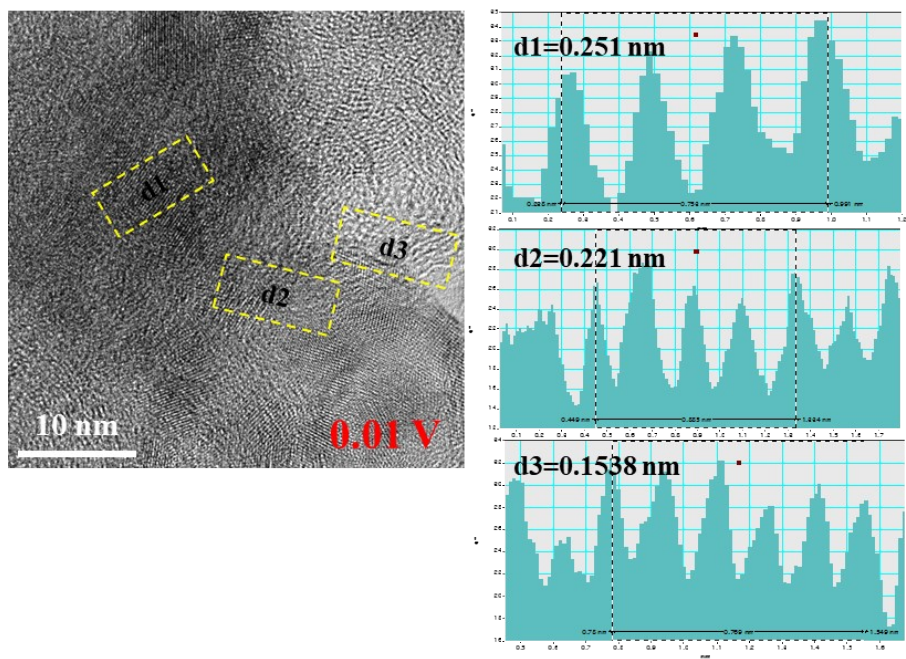
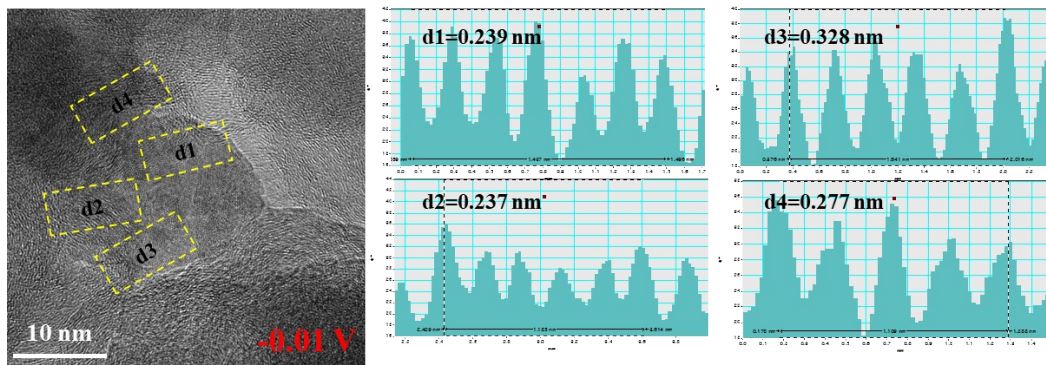**Figure S12.** The dQ/dV curves of the $d_mD_mL_m$, $d_sD_sL_l$ to $d_{xs}D_{xs}L_{xl}$ samples at 0.05 A g^{-1} from 0.005 V to 2.0 V.
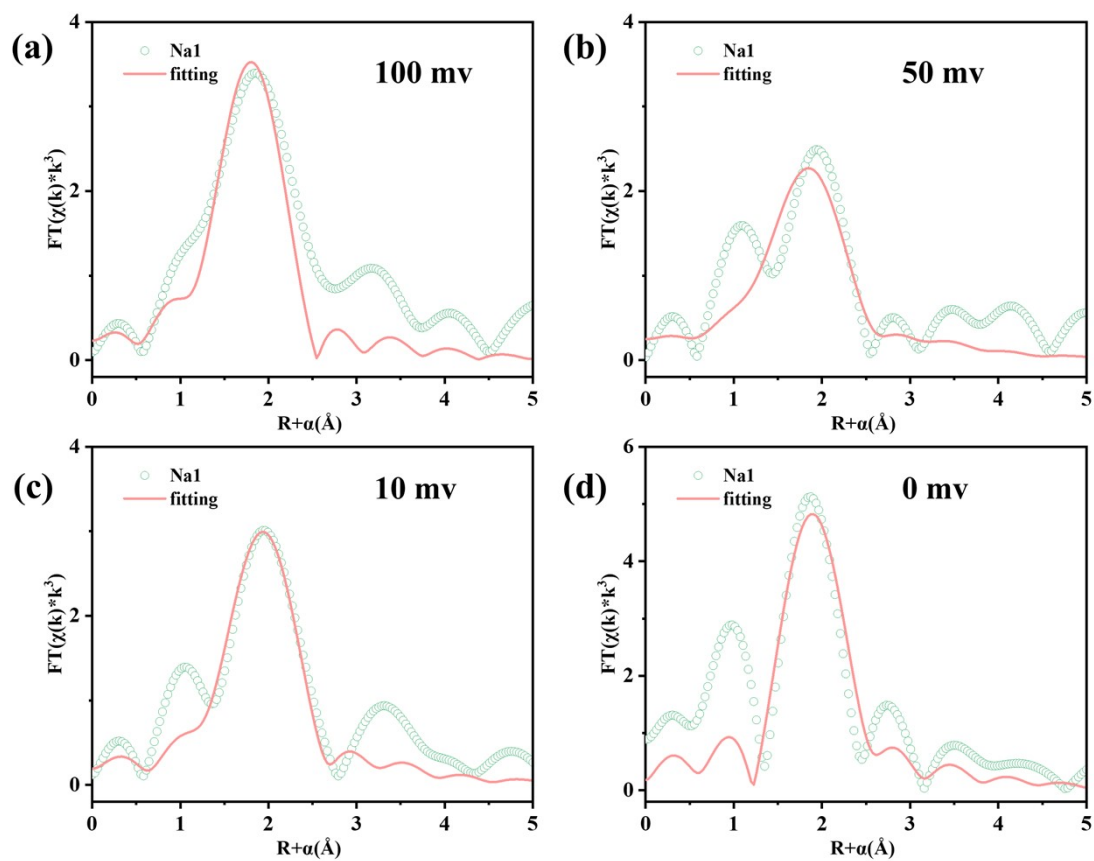
Figure S13. Ex-situ TEM images of $d_sD_sL_l$ electrode at different potentials of the sodization processes. (a) 0.5 V and (b) 0.1 V.

Figure S14. Ex-situ TEM images of $d_sD_sL_l$ electrode at different potentials of the sodization processes at 0.01 V.
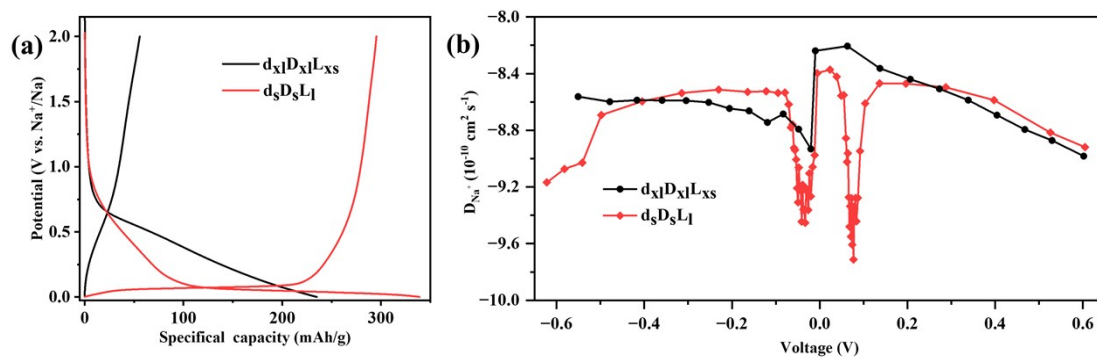
Figure S15. Ex-situ TEM images of $d_sD_sL_l$ electrode at different potentials of the sodization processes at -0.01 V.

Figure S16. (a-d) ex-situ synchrotron X-ray absorption spectroscopy of R spaces for $d_sD_sL_l$ electrode at different potentials of the sodization processes, (a) 100 mV, (b) 50 m V, (c) 10 mV, and (d) 0 mV.

Figure S17. (a) The discharge and charge curves at the first cycle, (b) and estimated sodium ions diffusion coefficients from the GITT potential profiles of the $d_{xl}D_{xl}L_{xs}$ and $d_sD_sL_l$ samples from 2.0 to 0.005 V.
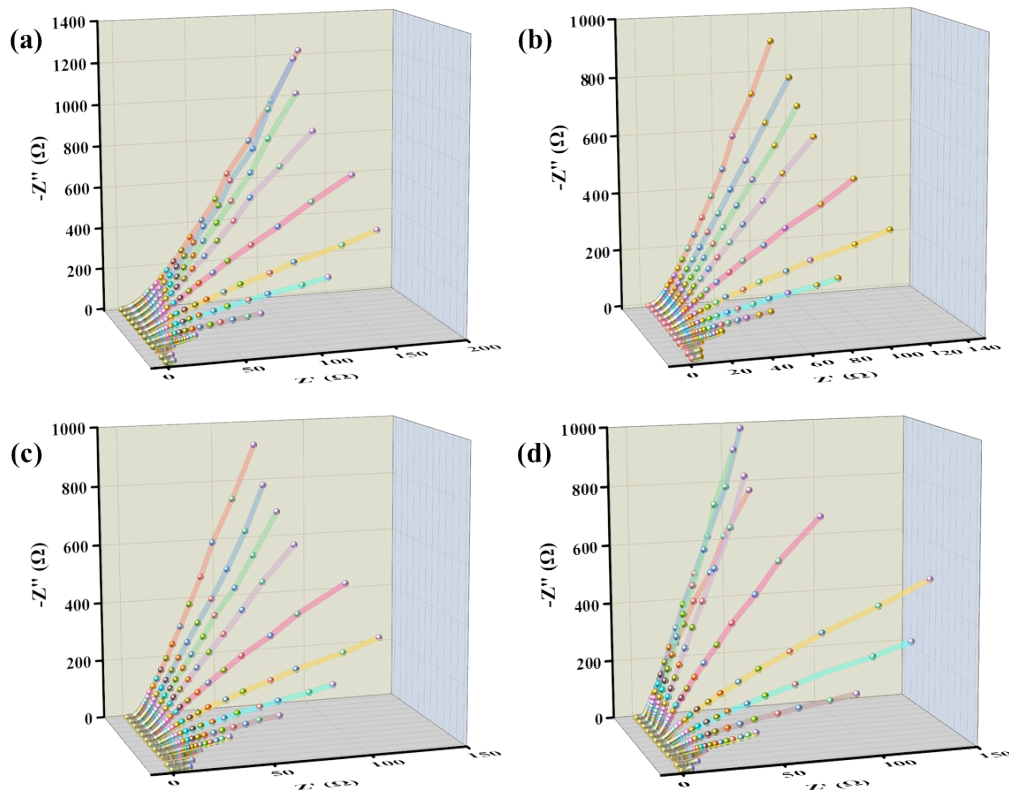
Figure S18. (a-d) *In-situ* Electrochemical impedance spectroscopy (EIS) curves of the $d_lD_lL_s$, $d_mD_mL_m$, $d_sD_sL_l$, and $d_{xs}D_{xs}L_{xl}$ samples at the discharging stage from 2.0 to 0.005 V.
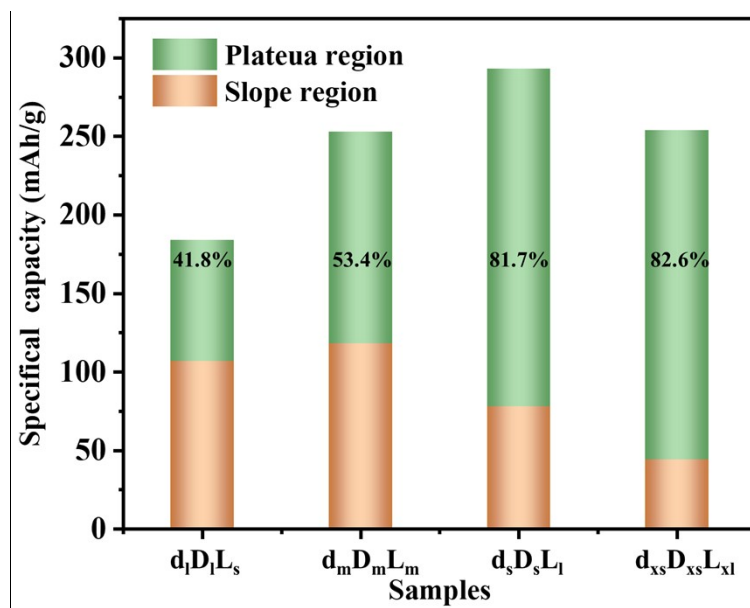
Figure S19. Contribution ratios of the slope capacity and plateau capacity of the $d_lD_lL_s$, $d_mD_mL_m$, $d_sD_sL_l$, and $d_{xs}D_{xs}L_{xl}$ samples in the 2nd cycle charge curves at 0.05 A g^{-1}.
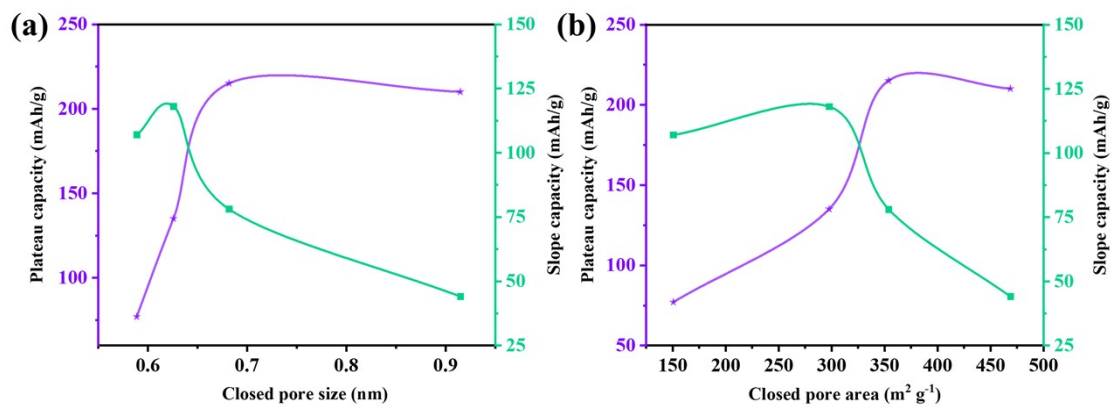
Figure S20. (a-b) Correlation between closed pore size, closed pore area and plateau capacity.

Table S1. The interlayer distance (d_{002}), average crystallite width (L_a), and average thickness (L_c) of graphite domains of X-ray diffraction (XRD) patterns for the $d_{xl}D_{xl}L_{xs}$, $d_lD_lL_s$, $d_mD_mL_m$, $d_sD_sL_l$, $d_{xs}D_{xs}L_{xl}$ samples.

Samples	d_{002}/nm	L_a/nm	L_c/nm
$d_{xl}D_{xl}L_{xs}$	0.394	2.69	0.762
$d_lD_lL_s$	0.389	2.79	0.88
$d_mD_mL_m$	0.384	3.35	1.037
$d_sD_sL_l$	0.382	3.68	1.059
$d_{xs}D_{xs}L_{xl}$	0.351	6.09	4.13

Table S2. The ratio of defects along the whole graphene sheets of the $d_{xl}D_{xl}L_s$, $d_mD_mL_m$, $d_sD_sL_l$, $d_{xs}D_{xs}L_{xl}$ samples.

Samples	$\dfrac{I_D}{I_D + I_G}$
$d_lD_lL_s$	0.9782
$d_mD_mL_m$	0.9327
$d_sD_sL_l$	0.9211
$d_{xs}D_{xs}L_{xl}$	0.8513

Table S3. Specific surface areas and pore structure by calculated from N_2 adsorption isotherms of the hard carbon.

Samples	Specifical surface area/ $m^2\ g^{-1}$	Total Volume/ $cm^{-3}\ g^{-1}$	Average pore size/nm
$d_l D_l L_s$	28.2	0.0297	8.37
$d_m D_m L_m$	4.1	0.009	5.27
$d_s D_s L_l$	4.0	0.009	4.61
$d_{xs} D_{xs} L_{xl}$	3.8	0.004	3.46

Table S4. EXAFS fitting result at the Na K-edge for the $d_sD_sL_l$ sample.

Sample	Shell	CN	R(Å)	ΔE_0(eV)	R factor
100 mV	Na-O	8.88	2.29	2.822	0.038
50 mV	Na-O	11.68	2.34	4.317	0.031
10 mV	Na-O	9.69	2.40	1.292	0.028
0 mV	Na-O	5.14	2.32	0.397	0.015

Note: It is important to note that the adjacent coordination structure exhibits a disordered trend around 100 mV, resulting in an unusual increase in the coordination number. With decreasing potential, the coordination number reveal the stable state, which is match up with the formation of smaller sodium clusters tends.

Table S5. Specific information for estimating sodium volume fraction and the closed pore volume.

Samples	C_{Na} (Plateau capacity/m Ah g^{-1})	D_{Na} (Sodium density /g cm^{-3})	$D_{v,Na}$ (Volumetric capacity of sodium/mA h cm^{-3})	Φ_{Na} (Sodium volume fraction/%)	Φ_{pore} (Closed pore volume/ g cm^{-3})
$d_lD_lL_s$	77	0.971	1132.19	0.066	0.053
$d_mD_mL_m$	135	0.971	1132.19	0.115	0.096
$d_sD_sL_l$	215	0.971	1132.19	0.184	0.179
$d_{xs}D_{xs}L_{xl}$	210	0.971	1132.19	0.180	0.233

Note: To determine the quantitative closed volume-pore relationship, we compared the sodium volume fraction (Φ_{Na}) filled by sodium metal/nanoclusters in the obtained hard carbon samples with the closed pore volume (Φ_{pore}) fitted by the SAXS data model. Based on the plateau capacity of completely fully sodiated hard carbon, Φ_{Na} is calculated by formula (6).

$$\Phi_{Na} = \frac{C_{Na} * D_{Na}}{C_{v,Na}} \tag{S6}$$

where C_{Na}, D_{Na}, and $C_{v,Na}$ are the experimentally obtained sodium plateau capacity, theoretical sodium density, and theoretical volumetric capacity of sodium, respectively.

References

1. J. Chen, E. Quattrocchi, F. Ciucci and Y. Chen, *Chem*, 2023, **9**, 2267-2281.
2. Y. Mo, W. Zhou, K. Wang, K. Xiao, Y. Chen, Z. Wang, P. Tang, P. Xiao, Y. Gong, S. Chen, P. Gao and J. Liu, *ACS Energy Lett.*, 2023, **8**, 995-1002.
3. M. Schönleber and E. Ivers-Tiffée, *Electrochemistry Communications*, 2015, **61**, 45-48.
4. G. Kresse and J. Hafner, *Physical Review B*, 1993, **47**, 558-561.
5. G. Kresse and J. Hafner, *Physical Review B*, 1994, **49**, 14251-14269.
6. G. Kresse and J. Furthmüller, *Computational Materials Science*, 1996, **6**, 15-50.
7. G. Kresse and J. Furthmüller, *Physical Review B*, 1996, **54**, 11169-11186.
8. J. Klimeš, D. R. Bowler and A. Michaelides, *Physical Review B*, 2011, **83**, 195131.
9. S. P. Ong, W. D. Richards, A. Jain, G. Hautier, M. Kocher, S. Cholia, D. Gunter, V. L. Chevrier, K. A. Persson and G. Ceder, *Computational Materials Science*, 2013, **68**, 314-319.
10. K. Momma and F. Izumi, *Journal of Applied Crystallography*, 2011, **44**, 1272-1276.